



Robust image segmentation and bias field correction model based on image structural prior constraint

Wenqi Zhao ^a, Jiacheng Sang ^b, Yonglu Shu ^{a,*}, Dong Li ^a

^a College of Mathematics and Statistics, Chongqing University, 401331, Chongqing, China

^b State Key Laboratory of Biotherapy, Sichuan University, 610000, Sichuan, China

ARTICLE INFO

Keywords:

Retinex
Adaptive bias correction
Image segmentation
Reflectance prior constraint
Binary level set

ABSTRACT

In this paper, we propose an advanced variational model for image segmentation and bias correction. In contrast to the majority of existing level set segmentation models that only consider illumination bias fields, we additionally consider the impact of image reflectance on segmentation accuracy. Our method is capable of effectively segmenting images with blurry edge structures affected by non-uniform illumination. In order to enhance segmentation efficiency, we directly segment the underlying structures of the images, construct spatial prior and apply adaptive regularization constraints on the structural component. Therefore, in the process of segmentation, the proposed algorithm can accurately identify object boundaries without being affected by the environment. Besides, the GL operator is applied to enhance the robustness of the model against noise. Furthermore, we use the alternating direction method of multipliers and the operator splitting algorithm for numerical solution. The experimental results obtained from various sorts of images illustrate that our model outperforms many leading-edge level set models with regard to robustness, corrected results and accuracy.

1. Introduction

In computer vision applications, image segmentation assumes a pivotal role. In practical applications, it is often used in combination with other fields of digital image processing, such as target detection (Bao et al., 2023; Obeso, Benois-Pineau, García Vázquez, & Álvaro Ramírez Acosta, 2022; Wen, Cheng, Fang, & Li, 2023), image denoising (Chen & Cheng, 2012; Wang, Zhao, & Ng, 2016), remote sensing image analysis (Lan, Shen, Zhang, & Yuan, 2014), image enhancement (Cai & Chen, 2023; Du et al., 2023; Jia, Wong, Wang, & Zeng, 2023) and so on. It is widely used in meteorological engineering, intelligent transportation, medical imaging, etc. The definition of image segmentation is to divide an image into several meaningful regions based on its features. However, due to variations in spatial illumination, defects in imaging equipment, and the influence of sensor material properties, the acquired images may encounter complex scenarios such as intensity inhomogeneity, illumination bias fields, and non-uniform noise. Therefore, it remains a challenge to extract regions of interest from the perspective of human visual perception. So far, a multitude of exceptional image segmentation models have been driving the advancement of image processing. In particular, region-based active contour models have received considerable interest due to their stability and adaptability. Among various types of region-based variational level set models, Mumford-Shah(MS) model has the widest range of

applications (Mumford & Shah, 1989). It continues to be extensively utilized in the fields of image segmentation, image denoising, and image restoration. The fundamental concept of the MS model is to pursue a piecewise smooth approximation for a given image. However, owing to the non-convexity and discontinuity of the unknown contours, the minimization of the MS energy functional becomes a challenging problem. Therefore, the active contours model without edges, known as the Chan-Vese (CV) model, was proposed by Chan and Vese (2001) for image segmentation. It can drive the evolution of the level set towards the target contour by exploiting the difference in image intensity inside and outside the curve. Because CV is a global active contour model, it is robust to noisy images. By assuming that the local intensity of the image follows a homogeneous distribution, Li, Kao, Gore, and Ding (2008) introduced a region-scalable fitting model that utilizes the local area intensity information of the image. An active contour model, known as LCV, was proposed by Wang, Huang, and Xu (2010), where the evolution of the level set is motivated by the global and local intensity details of the image. Wang, Zhang, Yang, Yi, and Chen (2020) used the entropy-weighted energy function as well as inhomogeneous entropy description operator to segment image with low contrast and intensity inhomogeneity while improving the segmentation efficiency. Yang, Wang, and Feng (2020) proposed a dynamic constraint term which can incorporate fuzzy clustering and level set

* Corresponding author.

E-mail addresses: zwq@stu.cqu.edu.cn (W. Zhao), sangjiacheng@stu.scu.edu.cn (J. Sang), shuyonglu@cqu.edu.cn (Y. Shu), lid@cqu.edu.cn (D. Li).

techniques for effective and fast controlling the evolution of curve. Liu, He, Gao, Wu, and Ren (2019) put forward a variational model in the framework of binary level sets, which employs the L_1 -norm metric for defining the data items, making up for the L_2 -norm metric data items which performs poorly in aspect of anti-noise capability. To segment convex shaped images, Luo, Tai, Huo, Wang, and Glowinski (2019) incorporated a convex image prior into a traditional level set model. Therefore, a segmentation model for occluded objects was proposed and this model is stable in terms of the parameters. Weng and Yan (2020) innovatively incorporated the concept of order-statistical filtering into the level set model. On the basis of the concept of maximum a posteriori probability theory, Cai, Liu, Zhou, Sun, and Li (2018) proposed adaptive-scale image segmentation model (ASACM) which is founded on image entropy, in which the new adaptive scale operator effectively enhances the image segmentation speed. There are many image segmentation models (Li, Cao, Wang, Cui, & Wang, 2020; Zhou, Wang, Zhang, Liang, & Gong, 2016; Zhu et al., 2021) which are built on the maximum a posteriori probability framework. With the intent of recovering the intensity inhomogeneity of an image caused by spatially varying illumination bias, the Retinex theory (Cheng, Huang, Zhao, Ma, & Huang, 2019; Du et al., 2023; Fu et al., 2015) has been proposed and applied to various fields of image processing. For instance, Ng and Wang (2011) proposed additive Retinex variational model for image enhancement. Besides, the Retinex theory has numerous contributions to image enhancement (Guo, Li, & Ling, 2017; Lan et al., 2014; Ren, Yang, Cheng, & Liu, 2020; Zhou et al., 2023). In recent years, some scholars have tried to integrate Retinex theory into the framework of level sets for image segmentation. Wang, Dong et al. (2016) incorporated the level set into the Total Variation model for Retinex model by decomposing the image into a sum of reflectance (also known as the structure) and illumination bias, utilizing the separation Bregman algorithm for fast image segmentation. However, the model iteration process is complex and time-consuming. Wu, Li, Zhang, and Liu (2018) proposed a variational image segmentation model which is grounded on the Retinex additive decomposition and makes a piecewise constant assumption on the reflectance. For the purpose of improving the data fidelity term of the CV model, Zosso et al. (2017) used the reflectance part S to replace the observed image I . Additionally, they imposed regularization constraints on the smoothness of the bias field. Based on this concept, Zosso et al. proposed the CVB model. Weng, Dong, and Lei (2021) considered the illumination bias field to be piecewise constant and proposed the additive bias correction segmentation (ABC) model. Although the CVB model, the model proposed by Wu et al., and the ABC model are all based on the theory of Retinex additive decomposition for image segmentation, they only considered the spatially smooth illumination bias field. Therefore, during the process of image segmentation, inaccurate segmentation and loss of detail often occur due to artifacts (Yang et al., 2023) and overexposure produced by the image bias correction process.

In this paper, based on the Retinex decomposition theory, we propose a new level set model for segmenting images with low contrast and intensity inhomogeneity, and concurrently estimating the bias field. As is well known, the reflectance of an image contains the intrinsic properties and texture structure of the object, which plays a crucial role in image edge orientation. Therefore, we utilize the reflectance information of the image to construct the spatial prior constraint, the constraint effectively improves the boundary quality of the corrected image. Additionally, we apply adaptive regularization constraints to the reflectance part based on the gradient information of the reflectance. This enables our method to adaptively correct illumination bias and preserve details when segmenting images with intensity inhomogeneity. Furthermore, to avoid the instability of traditional penalty terms and the complexity of re-initialization, and to increase the robustness of the model to noise, we introduce a GL-regularizer into the process of level set segmentation. The experimental results obtained from noisy, low contrast, low light, and MRI images certify the preponderance of proposed model over most image segmentation models with regard to corrected results, accuracy, and robustness.

2. Related work

2.1. Chan and Vese model

To further enhance the performance of the Mumford-Shah model, in the year 2001, Chan and Vese (2001) proposed a piecewise constant model that incorporates global intensity information. The following is the definition of the CV model:

$$E(c_1, c_2, \phi) = \lambda_1 \int_{\text{inside}(\Gamma)} (I - c_1)^2 dx + \lambda_2 \int_{\text{outside}(\Gamma)} (I - c_2)^2 dx + \alpha \cdot \text{length}(\Gamma) + \beta \cdot \text{area}(\text{inside}(\Gamma)), \quad (1)$$

where $I : \Omega \subset R^2 \rightarrow R$ represents the image domain. c_1 and c_2 correspond to the region-fitting information inside and outside the evolving curve Γ , separately. $\lambda_1, \lambda_2, \alpha, \beta$ are fixed positive parameters. In most experiments, they set $\lambda_1 = \lambda_2 = 1$. For the purpose of solving the minimization problem in Eq. (1), Chan and Vese proposed the use of a level set function ϕ instead of the contour curve Γ , and the image domain Ω is divided into the following two regions: $\text{inside}(\Gamma) = \{(x, y) \in \Omega, \phi(x, y) > 0\}$ and $\text{outside}(\Gamma) = \{(x, y) \in \Omega, \phi(x, y) < 0\}$. Therefore, the energy function $E(c_1, c_2, \phi)$ can be reformulated using the following level set formulation:

$$\begin{aligned} E^{CV}(c_1, c_2, \phi) = & \lambda_1 \int_{\Omega} (I - c_1)^2 H(\phi) dx + \lambda_2 \int_{\Omega} (I - c_2)^2 (1 - H(\phi)) dx \\ & + \alpha \int_{\Omega} \delta(\phi) |\nabla \phi| + \beta \int_{\Omega} H(\phi) dx, \end{aligned} \quad (2)$$

where $H(\phi)$ is the Heaviside function, $\delta(\phi)$ is the Dirac function, and ϕ represents the level set function. The CV model does not incorporate any local intensity details from the image. Consequently, although it may successfully detect weak boundaries in the image and exhibit some robustness to noisy images, it cannot effectively segment images with intensity inhomogeneity.

2.2. CVBS model

Based on the ability of the human visual system to perceive consistent colors under different lighting conditions, Land (1977) developed the Retinex model to explain color constancy phenomena. According to the Retinex theory, we can decompose an observed image i into the product of the illumination part b and the reflectance structure part s , as shown in Eq. (3):

$$i = bs. \quad (3)$$

By applying a logarithmic transformation, we can get $S = \log(s)$, $B = \log(b)$, and $I = \log(i)$, thus obtaining the following Eq. (4):

$$I = B + S, \quad (4)$$

where the illumination component B (Ma & Osher, 2012) varies smoothly and slowly. The edge details and texture of the image I are primarily determined by the structural component S . This is also a core assumption in most log-transformed Retinex models. Therefore, in accordance with the Retinex theory, the following CVBS model was proposed by Jin, Wu, Min, and Ng (2020) in their work, as shown in Eq. (5):

$$\begin{aligned} E_{CVBS}(c_1, c_2, \phi, B, S) = & \lambda_1 \int_{\Omega} (c_1 - S)^2 H(\phi) dx \\ & + \lambda_2 \int_{\Omega} (c_2 - S)^2 (1 - H(\phi)) dx \\ & + \gamma \int_{\Omega} |\nabla H(\phi)| dx + \tau \int_{\Omega} |\nabla S| dx + \nu \int_{\Omega} |\nabla B|^2 dx, \end{aligned} \quad (5)$$

which is designed for dynamic bias correction and image segmentation. $\lambda_1, \lambda_2, \gamma, \tau, v$ are positive parameters, and the definitions of c_1 and c_2 are the same as those in CV. The last regularization constraint is used to maintain the smoothness of the bias field. Although the CVBS model (Jin et al., 2020) has the capacity to simultaneously correct the illumination bias and perform image segmentation, when segmenting images with low contrast and severe noise, the CVBS model typically struggles to accurately identify image boundaries.

2.3. Binary level set

Lie, Lysaker, and Tai (2006) proposed a PDE-based image segmentation method known as the binary level set model. Unlike traditional level set methods which used signed distance function ϕ to implicitly represent the curve Γ , Lie et al. used a discontinuous level set function $\phi(x)$ to implicitly represent Γ . Its definition is as follows:

$$\phi(x) = \begin{cases} 1, & x \in \text{inside}(\Gamma) \\ -1, & x \in \text{outside}(\Gamma). \end{cases} \quad (6)$$

According to Eq. (6), Lie et al. proposed a binary level set image segmentation model. Lie et al. assumed that I is an image composed of the regions $\text{inside}(\Gamma)$ and $\text{outside}(\Gamma)$, and m serves as a piecewise constant approximation of I where m satisfies $m = c_1$ in the region $\text{inside}(\Gamma)$ and $m = c_2$ in the region $\text{outside}(\Gamma)$, i.e.,

$$m = c_1\eta_1 + c_2\eta_2, \quad (7)$$

$$\text{where } \eta_1 = \frac{1}{2}(1 + \phi), \eta_2 = \frac{1}{2}(1 - \phi).$$

Based on the assumptions mentioned above, Lie et al. proposed the following energy functional like Eq. (8):

$$F(c_1, c_2, \phi) = \frac{1}{2} \int_{\Omega} (I - m)^2 dx + \mu \int_{\Omega} |\nabla \phi| dx, \quad (8)$$

and minimized it to find the segmentation of a given image I . Here, $\mu \geq 0$ is a parameter used to control the regularization, and m is a piecewise constant function. By adding the constraint $\phi^2 = 1$, formulating the binary level set model Eq. (8) as a constrained minimization problem yields the following representation:

$$\min_{c_1, c_2, \phi} F(c_1, c_2, \phi), \phi^2 - 1 = 0. \quad (9)$$

For the goal of addressing this constrained minimization problem, Lie et al. proposed using the Lagrange projection method and augmented Lagrangian method, which transforms the problem Eq. (9) into the following energy functional:

$$L_{\mu}(c_1, c_2, \phi, \tau) = F(c_1, c_2, \phi) + \tau \int_{\Omega} (\phi^2 - 1) dx + \frac{1}{2} \mu \int_{\Omega} (\phi^2 - 1)^2 dx, \quad (10)$$

where $\tau > 0$ and $\mu > 0$ correspond to the augmented Lagrange multiplier and penalty parameter, respectively.

3. The proposed model

In this paper, we present an innovative concept of utilizing the structural information of images for image segmentation. We propose a novel spatial prior constraint term utilizing the reflectance of image. This term ensures that during simultaneous bias field correction and image segmentation, the correction results can be controlled within a prior range. As a result, it minimizes the interference of illumination factors on the segmentation results and improves the quality of the image after bias field correction. Compared to traditional level set segmentation priors (Yang, Shu, Wang, Feng, & Jia, 2020; Yang et al., 2021), when segmenting images with intensity inhomogeneity and low contrast, this term provides better correction of bias and edge localization. Then the prior constraint on reflectance is as follows:

$$\mathcal{R}(\chi, \chi_{pre}) = \tau \|\chi(S) - \chi_{pre}(S)\|^2 = \tau \int_{\Omega} |\chi(S) - \chi_{pre}(S)|^2 dx. \quad (11)$$

Here, $\tau > 0$, $\chi(S)$ represents the reflectance term in the Retinex model, and its definition is $\chi(S) = \exp(S)$. Then, Eq. (11) can be transformed into the following expression:

$$\mathcal{R}(\chi, \chi_{pre}) = \tau \|\chi(S) - \chi_{pre}(S)\|^2 = \tau \langle \exp(S) - \chi_{pre}(S), \exp(S) - \chi_{pre}(S) \rangle. \quad (12)$$

The definition of χ_{pre} is as follows:

$$\chi_{pre}(S) = \begin{cases} \frac{1}{2}, & S \in \Omega_1 \\ \infty, & \text{otherwise}, \end{cases} \quad (13)$$

where $\Omega_1 = \{x | x \in \mathbb{R}^{m \times n}, x_{i,j} \leq 0, \forall i, j\}$, $m \times n$ are the size of I , $i = 1, \dots, m, j = 1, \dots, n$.

Furthermore, in order to improve the periodic re-initialization process of the traditional level set function to a signed distance function, we introduce discontinuous binary level set functions into the CVBS data terms as a replacement for traditional level set functions. Then we obtain the following two-phase data fitting term:

$$E^{data}(c_1, c_2, \phi) = \lambda_1 \int_{\Omega} (c_1 - S)^2 (1 + \phi)^2 dx + \lambda_2 \int_{\Omega} (c_2 - S)^2 (1 - \phi)^2 dx. \quad (14)$$

In order to enhance the robustness of our algorithm against noise and effectively preserve details of the image, we improve the traditional length regularization term $\int_{\Omega} |\nabla H(\phi)| dx$ by replacing it with the H^1 -regularization term $\int_{\Omega} |\nabla \phi|^2 dx$. The H^1 -regularization term (Eseedoglu & Tsai, 2006) can effectively suppress oscillations in the level set function, further improving the accuracy of the model in segmenting images with severe noise. During the numerical solving process of Eq. (14), to guarantee that the level set ϕ remains a binary level set function, it is common to add the constraint $\phi^2 = 1$. Therefore, by introducing a penalty constraint, we transform the aforementioned minimization problem Eq. (14) into the following unconstrained minimization problem Eq. (15):

$$\min_{c_1, c_2, \phi, S} E(c_1, c_2, \phi, S) = E^{data}(c_1, c_2, \phi) + \mu \int_{\Omega} |\nabla \phi|^2 dx + \nu \int_{\Omega} (\phi^2 - 1)^2 dx + \mathcal{R}(\chi, \chi_{pre}), \quad (15)$$

where $\mu > 0$, $\nu > 0$, and ν is the penalty parameter. In the experimental process, it is regularly to choose a relatively large value for ν to penalize the deviation between ϕ^2 and 1. Compared to traditional level set segmentation models, during the iterative process, we employ a binary level set function, which can effectively avoid the complex process of re-initialization and improve the capacity of our model to accurately segment complex sharp corners in images.

Due to the influence of illumination bias, images can have diverse degrees of intensity inhomogeneity. Furthermore, the boundaries in images with severe intensity inhomogeneity are often blurry, and they may even be unidentifiable by the human visual system. Moreover, low-illuminated regions tend to have low contrast and correspond to smaller gradient magnitudes in an image with non-uniform lighting. Therefore, based on the gradient features of the reflectance, we establish an adaptive regularization parameter ω . Combining the above assumptions, the final energy functional is given by:

$$E(\phi, c_1, c_2, B, S) = E^{data}(c_1, c_2, \phi) + \mu \int_{\Omega} |\nabla \phi|^2 dx + \nu \int_{\Omega} (\phi^2 - 1)^2 dx + \alpha \int_{\Omega} |\nabla B|^2 dx + \beta \|\omega \circ \nabla S\|_1 + \mathcal{R}(\chi, \chi_{pre}), \quad (16)$$

where α and β are positive parameters and the fourth term represents a regularization constraint on the slowly varying illumination. \circ denotes the point-wise multiplication. The weight parameter ω is employed to

control the regularization strength of the reflectance. The definition can be stated as follows:

$$\omega(x) = \exp\left(-\frac{\|\nabla S(x)\|}{\sigma}\right), \quad (17)$$

where σ denotes the standard deviation which is defined by the gradient image of the reflectance, i.e., $\sigma = \text{std}(\|\nabla S\|)$. Each pixel in the image corresponds to a unique weight. When segmenting image with sharp or blurry boundaries, the relatively small weight ω which indicates weak regularization is assigned to maintain edge texture of the targets. However, in the interior regions of the image with severe intensity inhomogeneity, the relatively large weight which indicates strong regularization is used to recover the true intensity. Therefore, our model can adaptively correct the illumination bias of the image while simultaneously conducting image segmentation.

In the previous works (Wang, Dong et al., 2016; Wu et al., 2018; Zosso et al., 2017), most models only consider the influence of illumination bias field on segmentation and only applied an l_2 constraint to the illumination gradient term. However, the l_2 norm can often lead to blurry boundaries around regions with rapid changes in illumination. This can result in the quality of the reflectance map being affected by the blurry boundaries generated from the illumination part during the iterative process. As a result, the target boundaries of the corrected image can exhibit varying degrees of halo artifacts, which, in turn, can influence the precision of the segmentation.

Therefore, the combination of the proposed structural prior constraint and the adaptive regularization algorithm enhances the image quality and prevents segmentation errors caused by artifacts introduced during the process of image correction. We convert the aforementioned problem Eq. (16) into the following minimization problem:

$$\min_{\phi, c_1, c_2, B, S} E(\phi, c_1, c_2, B, S). \quad (18)$$

Below, we will demonstrate the process of solving the minimization problem of Eq. (16).

3.1. Algorithm implementation

In this section, we will utilize the split Bregman method (Goldstein & Osher, 2009), the alternating direction method of multipliers and the three-step splitting algorithm (Zhang, Zhang, Song, & Zhang, 2013) to solve Eq. (16). By introducing an auxiliary variable d , we can transform Eq. (16) into the following constrained optimization problem:

$$\begin{aligned} \min\{E^{\text{data}}(c_1, c_2, \phi) + \mu \int_{\Omega} |\nabla \phi|^2 dx + v \int_{\Omega} (\phi^2 - 1)^2 dx \\ + \alpha \int_{\Omega} |\nabla B|^2 dx + \beta \|\omega \odot d\|_1 + R(\chi, \chi_{\text{pre}})\}, \end{aligned} \quad (19)$$

which is subject to $I = B + S$, $\nabla S = d$. We also introduce the Lagrange multiplier θ to the linear constraints, where b is the Bregman parameter. The augmented Lagrangian function for Eq. (19) is determined by the following expression:

$$\begin{aligned} \mathcal{L}(d, c_1, c_2, \phi, B, S, b, \theta) = E^{\text{data}}(c_1, c_2, \phi) + \mu \int_{\Omega} |\nabla \phi|^2 dx \\ + v \int_{\Omega} (\phi^2 - 1)^2 dx \\ + \alpha \int_{\Omega} |\nabla B|^2 dx + \beta \|\omega \odot d\|_1 \\ + \tau \int_{\Omega} |\chi(S) - \chi_{\text{pre}}(S)|^2 dx \\ + \lambda \|d - \nabla S - b\|_2^2 + \frac{\rho}{2} \|I - B - S + \frac{\theta}{\rho}\|_2^2. \end{aligned} \quad (20)$$

Given the solution at iteration step k , which includes d^k , c_1^k , c_2^k , ϕ^k , B^k , S^k , b^k , and θ^k , we can update the solution of Eq. (19) using the split Bregman method, the alternating direction method of multipliers, and the three-step splitting algorithm.

Firstly, we update d^{k+1} , c_1^{k+1} , and c_2^{k+1} given ϕ^k , B^k , S^k , b^k , and θ^k . Therefore, we have:

$$(d^{k+1}, c_1^{k+1}, c_2^{k+1}) = \arg \min_{d, c_1, c_2} \mathcal{L}(d, c_1, c_2, \phi^k, B^k, S^k, b^k, \theta^k). \quad (21)$$

Specifically,

$$d^{k+1} = \text{shrink}(\nabla S + b^k, \frac{\beta \omega(S)}{2\lambda}), \quad (22)$$

where the shrinkage operator $\text{shrink}(x, \rho)$ can be found from the paper of Goldstein and Osher (2009). Similarly, c_1 and c_2 can be easily solved as follows:

$$c_1^{k+1} = \frac{\int_{\Omega} S^k (1 + \phi^k)^2 dx}{\int_{\Omega} (1 + \phi^k)^2 dx}, \quad c_2^{k+1} = \frac{\int_{\Omega} S^k (1 - \phi^k)^2 dx}{\int_{\Omega} (1 - \phi^k)^2 dx}. \quad (23)$$

In order to address the minimization problem for ϕ^{k+1} , given d^{k+1} , c_1^{k+1} , c_2^{k+1} , B^k , S^k , b^k , and θ^k , by employing the gradient descent method to Eq. (19), we obtain the subsequent level set evolution equation:

$$\frac{\partial \phi}{\partial t} = -\lambda_1(c_1^{k+1} - S^k)^2(1 + \phi) - \lambda_2(c_2^{k+1} - S^k)^2(\phi - 1) + \mu \Delta \phi - 2v\phi(\phi^2 - 1). \quad (24)$$

For the Eq. (24), we have the following initial values:

$$\phi(x, t)|_{t=0} = \phi^k(x),$$

and we will introduce the numerical solution method for this discrete equation. For convenience, we make the following assumptions:

$$A^k = \lambda_1(c_1^{k+1} - S^k)^2, \quad B^k = \lambda_2(c_2^{k+1} - S^k)^2.$$

Inspired by the Two-Step Splitting Method (TSSM) proposed by Zhang et al. (2013), we adopt it to numerically solve Eq. (24). The specific process involves iteratively solving the following three equations alternately until convergence is achieved.

Step 1: Solving the first part of Eq. (24):

$$\frac{\partial \phi}{\partial t} = -A^k(1 + \phi) + B^k(1 - \phi). \quad (25)$$

We start with the initial condition $\phi(x, t = 0) = \phi^k$ until a certain time T_1 to obtain $\phi^{k+1,1} = \phi(x, T_1)$ as the solution for the first step.

Step 2: Solving the third part of Eq. (24):

$$\frac{\partial \phi}{\partial t} = \mu \Delta \phi. \quad (26)$$

Based on the initial condition $\phi(x, t = 0) = \phi^{k+1,1}$, we obtain the solution for the second step, denoted as $\phi^{k+1,2} = \phi(x, T_2)$, where $T_2 > 0$ represents a certain time instant.

Step 3: Solving the second part of Eq. (24). Given the initial condition $\phi(x, t = 0) = \phi^{k+1,2}(x)$, we solve the following nonlinear equation:

$$\frac{\partial \phi}{\partial t} = -2v\phi(\phi^2 - 1). \quad (27)$$

We obtain the solution at the final time, $\phi^{k+1}(x) = \phi(x, T_3)$, where $T_3 > 0$ represents a certain time instant. Through the three steps described above, we have decomposed Eq. (24) into three sub-equations. Next, we will choose appropriate time steps to discretize these sub-equations and apply different methods to solve them:

$$\frac{\phi^{k+1,1} - \phi^k}{\tau_1} = -A^k(1 + \phi^{k+1,1}) + B^k(1 - \phi^{k+1,1}), \quad (28)$$

where $\tau_1 > 0$ is the time step size. Therefore, according to the implicit method, we have the following:

$$\phi^{k+1,1} = \frac{\phi^k - \tau_1(A^k - B^k)}{1 + \tau_1(A^k + B^k)}. \quad (29)$$

Similarly, we discretize Eq. (26) and obtain the following Poisson equation:

$$\frac{\phi^{k+1,2} - \phi^{k+1,1}}{\tau_2} = v \Delta \phi^{k+1,2}, \quad (30)$$

where $\tau_2 > 0$ is the time step size. By employing the fast Fourier transform, we derive the following expression:

$$\phi^{k+1,2} = \mathcal{F}^{-1}\left(\frac{\mathcal{F}(\phi^{k+1,1})}{1 - \mu\tau_2\mathcal{F}(\Delta)}\right). \quad (31)$$

In the third step, by analyzing the analytical solution of Eq. (27), we know that $\phi(x, t)$ approaches ± 1 as $t \rightarrow +\infty$. Thus, using the projection method, we obtain the following solution:

$$\phi^{k+1} = \begin{cases} 1 & \phi^{k+1,2} \geq 0 \\ -1 & \phi^{k+1,2} < 0. \end{cases} \quad (32)$$

Next, we update the variable B^k by solving for B^{k+1} given d^{k+1} , c_1^{k+1} , c_2^{k+1} , ϕ^{k+1} , S^k , b^k , and θ^k , as shown in Eq. (33):

$$\min_B \left\{ \alpha \int_{\Omega} |\nabla B|^2 dx + \frac{\rho}{2} \|I - B - S^k + \frac{\theta^k}{\rho}\|_2^2 \right\}. \quad (33)$$

The equivalent Euler–Lagrange equation is given by:

$$\rho B^{k+1} - 2\alpha\Delta B^{k+1} = \theta^k + \rho(I - S^k). \quad (34)$$

Utilizing the fast Fourier transform, we obtain the following:

$$B^{k+1} = \mathcal{F}^{-1}\left(\frac{\mathcal{F}[\rho(I - S^k) + \theta^k]}{\rho - 2\alpha\mathcal{F}(\Delta)}\right). \quad (35)$$

Updating S^{k+1} given d^{k+1} , c_1^{k+1} , c_2^{k+1} , ϕ^{k+1} , B^{k+1} , b^k , and θ^k , we solve for S^{k+1} as described by the following equation:

$$\begin{aligned} S^{k+1} = \arg \min \{ & \lambda_1 \int_{\Omega} (c_1^{k+1} - S)^2 (1 + \phi^{k+1})^2 dx \\ & + \lambda_2 \int_{\Omega} (c_2^{k+1} - S)^2 (1 - \phi^{k+1})^2 dx \\ & + \lambda \|d^{k+1} - \nabla S - b^k\|_2^2 + \frac{\rho}{2} \|I - B^{k+1} - S + \frac{\theta^k}{\rho}\|_2^2 \\ & + \tau \int_{\Omega} |\chi(S) - \chi_{pre}(S)|^2 dx \}. \end{aligned} \quad (36)$$

The Euler–Lagrange equation corresponding to Eq. (36) is as follows:

$$\begin{aligned} 2\lambda_1 S^{k+1} (1 + \phi^{k+1})^2 + 2\lambda_2 S^{k+1} (1 - \phi^{k+1})^2 + \rho S^{k+1} - 2\lambda \Delta S^{k+1} \\ = \rho(I - B^{k+1}) + \theta^k + 2\lambda_1 c_1^{k+1} (1 + \phi^{k+1})^2 + 2\lambda_2 c_2^{k+1} (1 - \phi^{k+1})^2 \\ + 2\lambda (\nabla(b^k - d^{k+1})) - 2\tau(\chi(S) - \chi_{pre}(S))\chi(S). \end{aligned} \quad (37)$$

In typical numerical experiments, λ_1 and λ_2 are usually set to be equal. By utilizing the fast Fourier transform, we can obtain Eq. (38):

$$\begin{aligned} S^{k+1} = \\ \mathcal{F}^{-1}\left(\frac{\mathcal{F}[f^{k+1} + \rho(I - B^{k+1}) + \theta^k + 2\lambda(\nabla(b^k - d^{k+1})) - 2\tau(\chi(S) - \chi_{pre}(S))\chi(S)]}{2\lambda_1(1 + \phi^{k+1})^2 + 2\lambda_2(1 - \phi^{k+1})^2 + \rho - 2\lambda\mathcal{F}(\Delta)}\right), \end{aligned} \quad (38)$$

where we set $f^{k+1} = 2\lambda_1 c_1^{k+1} (1 + \phi^{k+1})^2 + 2\lambda_2 c_2^{k+1} (1 - \phi^{k+1})^2$. The remaining variables are updated as follows:

$$b^{k+1} = b^k + (\nabla S^{k+1} - d^{k+1}), \quad (39)$$

and

$$\theta^{k+1} = \theta^k + \rho(I - B^{k+1} - S^{k+1}). \quad (40)$$

The algorithm for solving the above model Eq. (16) is as follows:

Algorithm 1 Solver for Eq. (16)

1. Given initial values: $S^0 = I$, $B^0 = 0$, $d^0 = 0$, $\theta = 0$, $b = 0$;

2. Iterate and update as follows:

$$\begin{aligned} d^{k+1}, c_1^{k+1}, c_2^{k+1}, \phi^{k+1}, B^{k+1}, S^{k+1}, b^{k+1}, \theta^{k+1}, \\ d^{k+1} = \text{shrink}(\nabla S + b^k, \frac{\rho\alpha(S)}{2\lambda}), \\ c_1^{k+1} = \frac{\int_{\Omega} S^k (1 + \phi^k)^2 dx}{\int_{\Omega} (1 + \phi^k)^2 dx}, \quad c_2^{k+1} = \frac{\int_{\Omega} S^k (1 - \phi^k)^2 dx}{\int_{\Omega} (1 - \phi^k)^2 dx}, \\ \phi^{k+1,1} = \frac{\phi^k - \tau_1(A^k - B^k)}{1 + \tau_1(A^k + B^k)}, \\ \phi^{k+1,2} = \mathcal{F}^{-1}\left(\frac{\mathcal{F}(\phi^{k+1,1})}{1 - \mu\tau_2\mathcal{F}(\Delta)}\right), \\ B^{k+1} = \mathcal{F}^{-1}\left(\frac{\mathcal{F}[\rho(I - S^k) + \theta^k]}{\rho - 2\alpha\mathcal{F}(\Delta)}\right), \\ S^{k+1} = \\ \mathcal{F}^{-1}\left(\frac{\mathcal{F}[f^{k+1} + \rho(I - B^{k+1}) + \theta^k + 2\lambda(\nabla(b^k - d^{k+1})) - 2\tau(\chi(S) - \chi_{pre}(S))\chi(S)]}{2\lambda_1(1 + \phi^{k+1})^2 + 2\lambda_2(1 - \phi^{k+1})^2 + \rho - 2\lambda\mathcal{F}(\Delta)}\right), \\ b^{k+1} = b^k + (\nabla S^{k+1} - d^{k+1}), \\ \theta^{k+1} = \theta^k + \rho(I - B^{k+1} - S^{k+1}). \end{aligned}$$

3. Iterate until convergence is reached.

4. Experimental results

To further assess the performance of our algorithm and demonstrate the efficiency of our method, in this section, we conducted extensive experimental studies. In the subsequent experiments, we have established a maximum limit of 25 iterations. In most of the experiments, we set $\lambda_1 = \lambda_2 = \tau$. The smoothing parameter α is adjusted in accordance with the estimated smoothness of the bias field. The parameter β varies within the range of [0.5, 3]. The range of variation for α is set to [150, 500]. The range of variation for ρ is set to [0.75, 4]. The range of variation for τ_1 is set to [50, 400]. The numerical performance of our algorithm is not significantly influenced by the choice of λ . Therefore, we fix λ at 0.001. Furthermore, to facilitate parameter tuning, we fix $\mu = \beta$ and $\tau_2 = 2\rho$. In the following discussion, we will select different parameters based on the types of images. To quantify our experimental results, we used five evaluation metrics: Dice, IoU, Accuracy, JS and VOE. The specific definitions of these metrics are as follows:

$$\text{Dice} = \frac{2 * \text{TP}}{\text{TP} + \text{FP} + \text{TN} + \text{FN}}, \quad (41)$$

$$\text{IoU} = \frac{\text{TP}}{\text{TP} + \text{FP} + \text{FN}}, \quad (42)$$

$$\text{Accuracy} = \frac{\text{TP} + \text{TN}}{\text{TP} + \text{TN} + \text{FP} + \text{FN}}, \quad (43)$$

$$\text{JS} = \frac{\text{TP}}{\text{TP} + \text{FP}}, \quad (44)$$

$$\text{VOE} = 1 - \frac{\text{TP}}{\text{TP} + \text{FP}}, \quad (45)$$

where TP represents true positive, and TN represents true negative corresponding to the regions that are correctly segmented and unsegmented. FP represents false positive, and FN represents false negative. They respectively correspond to the false regions that are correctly detected and the actual regions that are undetected. The Dice coefficient is a measure of set similarity and is widely employed to measure the similarity between two samples. IoU represents the proportion of overlap between different images. The proportion of accurately predicted results out of the total samples is quantified by Accuracy. JS is employed for comparing the similarity and dissimilarity between finite sets of samples. VOE is calculated using the ratio between intersection and union between two sets of segmentations.

In the experiment, we compared the following models: ABC model (Weng et al., 2021), DRLSE-ADMM model (Wali, Li, Imran, Shakoor, & Basit, 2023), ICTM model (Wang & Wang, 2022), HLFRA model (Fang, Liu, Zhang, Liu, & Liu, 2021), ALF model (Ma, Liao, Chen, Liao, & Ma, 2019), DRLSE model (Li, Xu, Gui, & Fox, 2010), LSACM model (Zhang, Zhang, Lam, & Zhang, 2016), and LBF model (Li et al., 2008). We

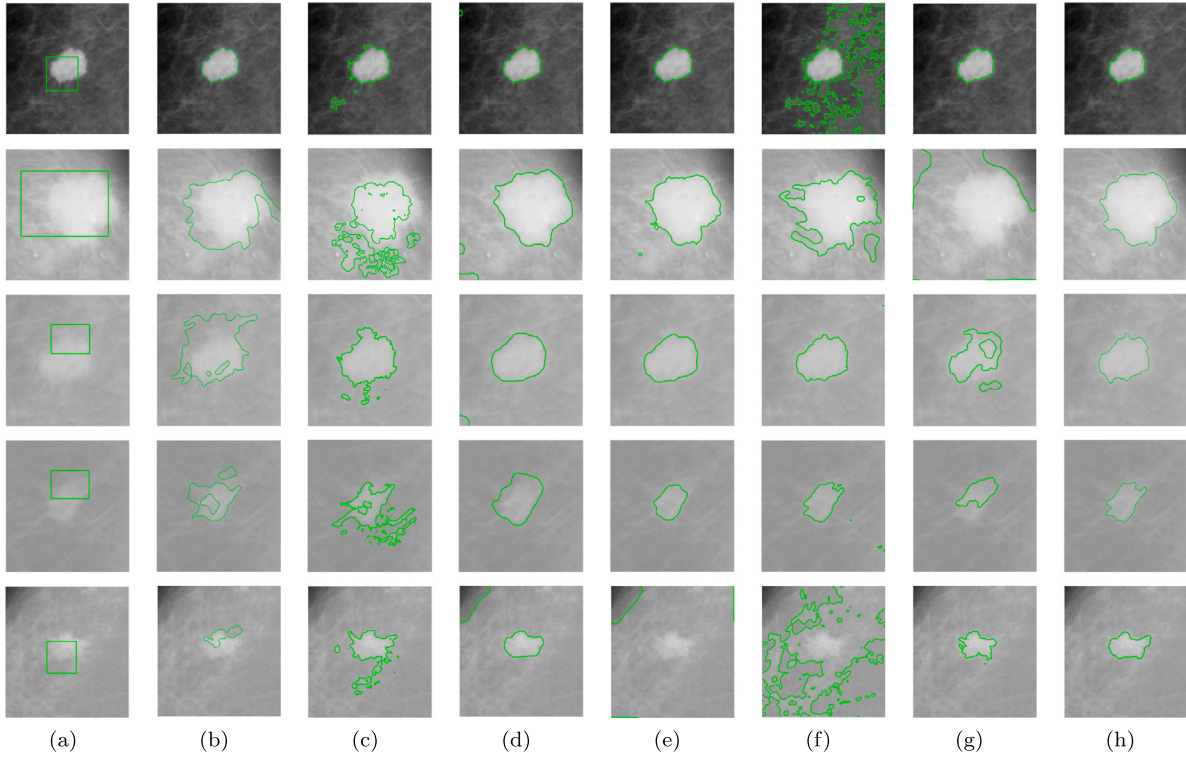


Fig. 1. Segmentation of five different low-contrast images is performed using the ABC model, the LSACM model, the LBF model, the DRLSE-ADMM model, the HLFRA model, the ALF model and the proposed model. The images above, from left to right, correspond to the original low-contrast images with initial contours, the segmentation results of the ABC model, the LSACM model, the LBF model, the DRLSE-ADMM model, the HLFRA model, the ALF model and the proposed model for low-contrast image segmentation.

designed a total of nine comparative experiments, which fully demonstrated the excellent capabilities of our models with respect to segmentation robustness, segmentation efficiency, and accuracy in various scenarios, including low contrast, low lighting, natural images, medical images, noisy images, and synthetic images with bias fields.

4.1. Low-contrast image

For the purpose of validating the superiority of the underlying structure of the segmentation in handling low-contrast images, we compared our model with the ABC, LSACM, LBF, DRLSE-ADMM, HLFRA, and ALF methods to evaluate their performance in handling low-contrast images. We set the parameters as follows: $\lambda_1 = \lambda_2 = \tau = 1$, $\tau_1 = 200$, $\beta = 1$, $\rho = 3$, and $\alpha = 500$. Fig. 1 displays five low-contrast digital mammography images. From left to right, the images correspond to the original low-contrast images with initial contours, the segmentation results of other comparative models and that of our model. From the images, it is evident that there is a significant similarity in intensity values among the background and the white masses. Furthermore, the boundaries of the white masses appear to be relatively blurred. Therefore, accurately capturing the lesions and preserving the object boundaries are challenging tasks. From the experimental results, it can be observed that when there is a significant contrast between the target and the background, most models can accurately segment the target. However, when the image contrast is reduced, it is apparent that the DRLSE-ADMM model and the ABC model can only detect a partial region of interest but fail to provide the desired boundaries. The LSACM and LBF models, although capable of locating the image boundaries, tend to segment out unnecessary or excessive parts. In addition, both the ALF and HLFRA models are far less accurate and stable in segmenting low-contrast images compared to the proposed model. That's because our model employs the reflection structure term

of the image to guide the identification of image boundaries. So the experimental results unequivocally establish that our model outperforms other models with respect to segmentation accuracy.

4.2. Low-light images

Detailed texture information is prominently presented within the reflectance part of the Retinex framework, and the regularization constraint on the reflectance component has a significant impact on the restoration of low-light images. As a result, in this experiment, we designed the following experiments to substantiate the outstanding performance of our algorithm in segmenting low-light images. We set the parameters as follows: $\rho = 1.2$, $\lambda_1 = \lambda_2 = \tau$ and within the range of [0.9, 1.4]. The parameter τ_1 varies within the range of [80, 150]. The parameter β varies within the range of [0.5, 3]. The range of variation for α is set to [200, 500]. Fig. 2 displays five low-light images from the initial row up to the fifth row. From the experimental results, it is apparent from the observations that the ABC model, which relies on the Retinex additive theory has certain advantages in recognizing object boundaries. However, it still suffers from details being lost and the inability to identify multiple objects. The segmentation accuracy is much lower compared to the proposed model. On the other hand, the LSACM, LBF, and DRLSE-ADMM models based on other assumptions are heavily affected by the low contrast in the images, making it difficult to attain precise object boundary extraction. Fig. 3 presents the box plot of the segmentation results shown in Fig. 2. Our method takes into consideration both the prior constraints on the reflectance and the adaptive regularization of the reflectance. As a result, it demonstrates significant advantages in boundary localization and detail preservation.

4.3. Real images

Fig. 4 illustrates the segmentation performance of our algorithm in comparison to other comparative algorithms on eight natural images.

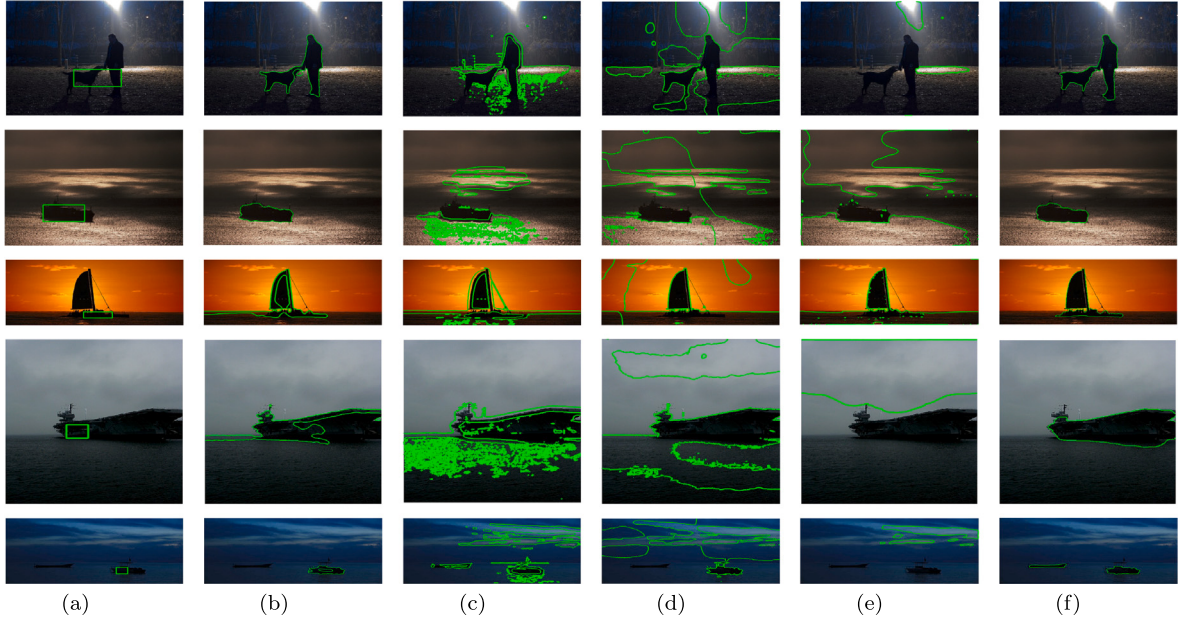


Fig. 2. The segmentation of five distinct low light images is performed using the ABC model, the LSACM model, the LBF model, the DRLSE-ADMM model, and the proposed model. The images above, from left to right, correspond to the original low light images with initial contours, the segmentation results of the ABC model, the LSACM model, the LBF model, the DRLSE-ADMM model, and the proposed model for low light images.

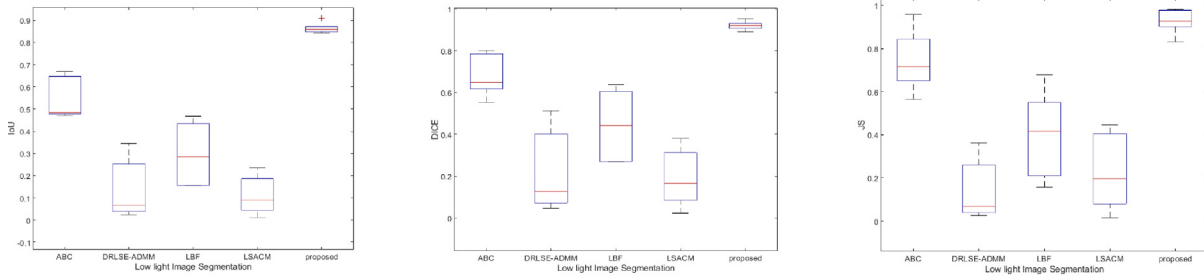


Fig. 3. The findings of our quantitative comparison experiments on Dice, IoU, JS values for low light images in Fig. 2.

We set the parameters as follows: $\lambda_1 = \lambda_2 = \tau = 1$, $\tau_1 = 300$, $\beta = 1.2$, $\rho = 3$, and $\alpha = 200$. The leftmost column represents the original images intended for segmentation, while the second column displays the ground truth (GT) images. The segmentation results of the comparative models are displayed in the third to sixth columns. We have numbered the eight images and used the same initial contours for the experiments to ensure fairness. It is noticeable that most models may recognize the boundaries of the objects. However, as images in row (2), (3), and (6) of Fig. 4 show, if there are interfering factors in the background, the comparative models may exhibit error segmentation. In row (7), the ABC model, the LSACM model, and the LBF model have misclassified some foreground details as background. Similarly, in row (3) and (8), the background texture of the images has been misclassified as foreground. For the purpose of evaluating the segmentation performance, we intend to perform a quantitative evaluation of the segmentation results and compare the CPU time among different models. Among all the comparative models, as illustrated in Table 1, our model exhibits the highest average values for Dice, IoU, and Accuracy. Furthermore, in terms of runtime, as illustrated in Table 2, our model has the least average CPU time. This further confirms that not only does the proposed model demonstrate exceptional accuracy in segmentation, but it also stands out as the most efficient.

4.4. MRI images with added bias field

To verify the robustness of our method to various degrees of bias fields, we respectively added bias fields of 20%, 40%, and 60% to brain tumor images. We set the parameters as follows: $\lambda_1 = \lambda_2 = \tau = 1$, $\tau_1 = 50$, $\beta = 2$, $\rho = 1.2$, and $\alpha = 500$. Fig. 5 depicts the images with added bias fields and their corresponding segmentation results. It is noticeable that our method maintains a consistent segmentation accuracy when segmenting images that contain varying degrees of bias fields. The JS values corresponding to the segmentation results are plotted as a Table 3. It shows that the JS values obtained from the segmentation results remain stable around 0.963 with minor fluctuations. Our model employs the gradient information of reflectance to construct adaptive weights. When the image bias field changes, the regularization strength of reflectance will also change accordingly. Therefore, our method has the capacity to capture edge details well in images with intensity inhomogeneity.

4.5. Medical images

As computer-aided technologies for medical diagnosis and treatment continue to evolve, medical image segmentation has been widely

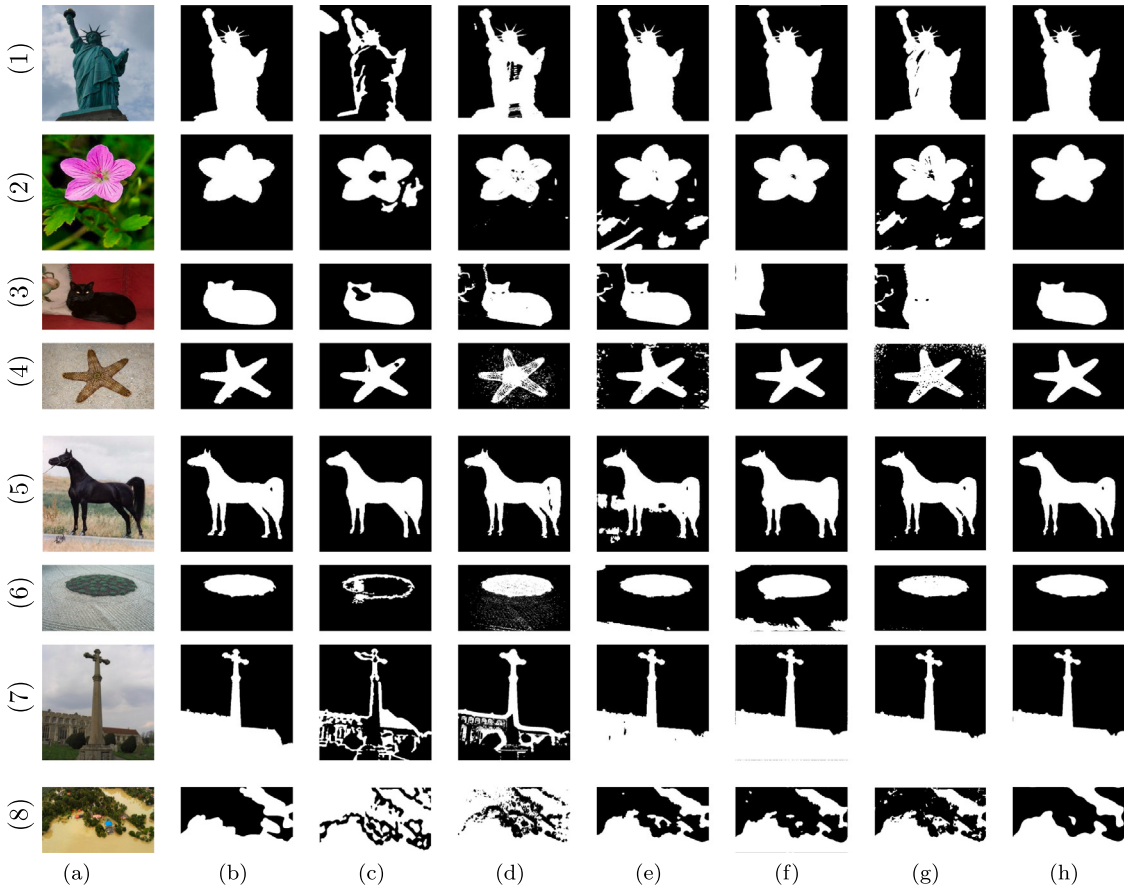


Fig. 4. A comparative analysis is conducted on the segmentation results of the ABC model, the LSACM model, the LBF model, the DRLSE-ADMM model, HLFRA model, and our model. The images above, from left to right, consist of the original images, the ground truths, the segmentation results of the ABC model, the LSACM model, the LBF model, the DRLSE-ADMM model, the HLFRA model, and the proposed model.

Table 1
The findings of our quantitative comparison experiments on Dice, IoU, Accuracy values for 8 real images in Fig. 4.

Parameter	Image	Model						
			ABC	LSACM	LBF	DRLSE-ADMM	HLFRA	OURS
Dice	(1)	0.5603	0.9438	0.9544	0.9916	0.9807	0.9950	
	(2)	0.9019	0.9767	0.8056	0.9831	0.8774	0.9855	
	(3)	0.9062	0.9123	0.8871	0.0066	0.0305	0.9452	
	(4)	0.9460	0.8668	0.8675	0.9784	0.8881	0.9650	
	(5)	0.9685	0.8663	0.9753	0.9505	0.9726	0.9754	
	(6)	0.4421	0.8900	0.8182	0.7056	0.9672	0.9867	
	(7)	0.4604	0.5286	0.9553	0.9780	0.9672	0.9806	
	(8)	0.7151	0.7251	0.9004	0.9045	0.9047	0.9336	
	Mean	0.7375	0.8523	0.8818	0.8123	0.8255	0.9709	
IoU	(1)	0.3891	0.8936	0.9128	0.9833	0.9621	0.9900	
	(2)	0.8214	0.9545	0.6745	0.9667	0.7816	0.9715	
	(3)	0.8284	0.8387	0.7970	0.0033	0.0155	0.9323	
	(4)	0.8975	0.7650	0.7661	0.9576	0.7987	0.9323	
	(5)	0.9389	0.9617	0.7641	0.9057	0.9467	0.9519	
	(6)	0.2838	0.8017	0.6923	0.5451	0.9365	0.9737	
	(7)	0.2991	0.3592	0.9145	0.9573	0.9658	0.9619	
	(8)	0.5566	0.5688	0.8189	0.8256	0.8261	0.8755	
	Mean	0.6269	0.7665	0.7925	0.7680	0.7791	0.9441	
Accuracy	(1)	0.7823	0.9654	0.9693	0.9946	0.9878	0.9968	
	(2)	0.9567	0.9900	0.8990	0.9928	0.9453	0.9938	
	(3)	0.9469	0.9464	0.9290	0.5974	0.5314	0.9678	
	(4)	0.9796	0.8937	0.9390	0.9915	0.9531	0.9866	
	(5)	0.9851	0.9883	0.9254	0.9757	0.9871	0.9884	
	(6)	0.8635	0.9602	0.9268	0.8634	0.9894	0.9956	
	(7)	0.7025	0.9081	0.9652	0.9834	0.9867	0.9853	
	(8)	0.7263	0.7496	0.9796	0.9709	0.9024	0.9730	
	Mean	0.85525	0.9118	0.9313	0.9133	0.9104	0.9810	

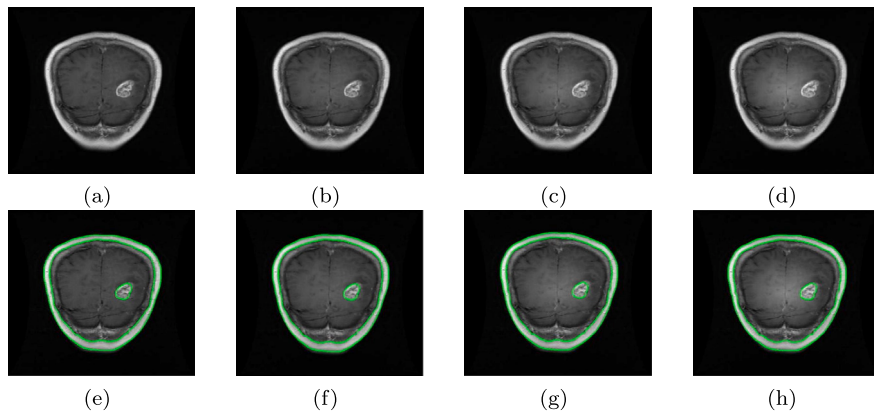


Fig. 5. Our model was utilized to accurately segment four brain MR images, which were subject to varying degrees of bias fields. From the first column to the fourth column, they correspond to original brain MR images, brain MR images with 20% bias field added, brain MR images with 40% bias field added and brain MR images with 60% bias field added and their corresponding segmentation results.

Table 2

The findings of our quantitative comparison experiments on CPU times for 8 real images in Fig. 4.

Image	Model					
	ABC	LSACM	LBF	DRLSE-ADMM	HLFRA	OURS
(1)	11.01	36.70	4.73	8.71	3.60	2.93
(2)	5.60	20.53	3.70	1.87	2.65	2.40
(3)	4.20	29.30	18.18	2.18	4.80	2.58
(4)	4.13	2.98	16.13	2.10	1.90	2.80
(5)	5.30	19.02	8.08	4.13	2.42	2.50
(6)	6.19	30.32	11.35	13.13	3.21	2.78
(7)	7.63	83.34	1.64	11.74	1.71	1.82
(8)	11.40	20.55	30.33	8.69	2.75	2.46
Mean	6.93	30.34	13.02	6.57	2.88	2.53

Table 3

The JS values generated by our method for the images illustrated in Fig. 5.

Image	(e)	(f)	(g)	(h)
JS	0.9635	0.9630	0.9624	0.9631

applied in medical research, clinical diagnosis, lesion analysis, and other fields. The purpose of medical segmentation is to extract lesions or identify abnormalities from MRI and CT images, providing a basis for further clinical research. However, medical image segmentation remains a complex and demanding mission due to the diversity of medical images and the influences of factors such as noise, tissue motion, and bias fields during the imaging process. In order to further verify the segmentation efficiency and performance of our model on medical images, in this experiment, we conducted qualitative and quantitative analysis on four MRI images. We set the parameters as follows: $\lambda_1 = \lambda_2 = \tau = 1$, $\tau_1 = 200$, $\beta = 1$, $\rho = 1.5$, and $\alpha = 200$. Fig. 6 illustrates the segmentation results. From a visual perspective, in the brain tumor images of the first and fourth rows, although the LSACM, LBF, DRLSE-ADMM, HLFRA, and ICTM models can locate the boundaries of the target, they are influenced by the brighter areas of the skull and exhibit over-segmentation. Simultaneously, because of the fuzzy nature of the tumor edge region, within the image, specifically in the fourth row, the ABC model exhibits under-segmentation. In particular, for the brain CT images shown in the second row, it can be observed that the LBF, LSACM, HLFRA and ICTM models successfully segment the target region, but most of them fail to segment some gray matter sulci. In comparison, the proposed model demonstrates higher accuracy in segmenting medical images. Fig. 7 presents the line graphs of the quantitative metrics for the aforementioned four images. From the graph, the results indicate that our algorithm exhibits the

highest JS and Dice values, which are also highly stable. Additionally, our algorithm generates a VOE line graph that is closer to 0. This validates the efficiency of our algorithm in segmenting MRI images. To further demonstrate the accuracy of our model in medical tumor image segmentation, we conducted experiments as depicted in Fig. 8. It presents the outcomes of the ABC model, the LBF model, the ICTM model, the DRLSE model, the ALF model, and our model for segmenting 16 brain tumor MRI images. In this section, we provide the parameter selection for segmenting the 16 512*512 brain tumor images. Among them, λ_1 and λ_2 are parameters used to balance the energy inside and outside the level set contour. It is typically set as $\lambda_1 = \lambda_2$, and in our experiments, we set $\lambda_1 = \lambda_2 = \tau$. Regarding the parameters β and μ , they correspond to the adaptive regularizer for reflectance and the H^1 -regularization coefficient proposed in our model. For the images in column (f), (d), (e), (f), (g), and (m) in Fig. 8, in order to reduce the influence of high-intensity regions at the skull edges on tumor segmentation and minimize oscillations during the curve evolution process, we have opted for larger regularization parameters. Therefore, we set the parameters $\beta = \mu = 5$ for these images. For the remaining images, we set $\beta = \mu = 1.5$. During the process of solving the level set function, we employed an implicit solving method. As a result, we can choose a larger time step τ_1 to accelerate the evolution of the level set. In our experiments, we set $\tau_1 = 50$. For brain tumor images affected by certain illumination variations, we set the regularization parameter for the illumination variation field to 150. The remaining parameter ρ was fixed at 1.5. In Table 4, the Dice values and the JS values for segmenting the 16 brain tumor images are presented for our model and the aforementioned four models. The experimental findings indicate that our model exhibits remarkable performance and stable segmentation accuracy in segmenting tumor images.

4.6. Noisy images

Whether they are low-light images, medical images, or real-world images or not, they all contain various levels of intensity inhomogeneity and noise. This necessitates that the proposed algorithm has a certain level of robustness to handle noisy and unevenly illuminated images. To verify the segmentation accuracy of our model on images with severe noise, the subsequent experiment was devised. We set the parameters as follows: $\lambda_1 = \lambda_2 = \tau = 1.05$, $\tau_1 = 150$, $\beta = 2.6$, $\rho = 2.6$, and $\alpha = 450$. Based on the different intensities of noise, we can fine-tune some parameters to achieve better segmentation results. From the first column to the last column in Fig. 9, they respectively show the original image accompanied by the initial contour, the segmentation outcome for the original image, and the segmentation result after adding the same type of noise. The rows depicted in Fig. 9 illustrate three distinct

Table 4

The Dice coefficient and the JS values for quantitative comparison experiments on 16 brain tumor images of size 512*512 are depicted in Fig. 8.

Criteria	Dice					JS							
	Images	ABC	ICTM	LBF	ALF	DRLSE	Proposed	ABC	ICTM	LBF	ALF	DRLSE	Proposed
(a)	0.9576	0.9611	0.8739	0.9059	0.8087	0.9618	0.9973	0.9906	0.9013	0.8449	0.9966	0.9679	
(b)	0.9755	0.9721	0.9444	0.8183	0.9694	0.9532	0.9806	0.9749	0.9257	0.8327	0.9769	0.9648	
(c)	0.9747	0.9093	0.9478	0.7691	0.9283	0.9371	0.9903	0.8619	0.9282	0.9482	0.9906	0.9555	
(d)	0.5879	0.7463	0.4562	0.6981	0.8561	0.9067	0.6447	0.8213	0.5265	0.6789	0.9905	0.9434	
(e)	0.7681	0.2106	0.3546	0.5428	0.6012	0.9009	0.6579	0.244	0.5321	0.6542	0.4298	0.9506	
(f)	0.9335	0.7979	0.7359	0.8369	0.8387	0.8925	0.9951	0.7526	0.7201	0.8273	0.9013	0.9985	
(g)	0.7135	0.7037	0.7028	0.9003	0.7433	0.9087	0.7895	0.8174	0.6526	0.8706	0.9012	1	
(h)	0.9201	0.9256	0.9034	0.9071	0.9178	0.9242	1	0.9937	0.9132	0.9152	0.9978	0.9174	
(i)	0.7977	0.7936	0.9175	0.8645	0.6972	0.9202	1	0.8808	0.8808	0.7676	0.5701	0.9742	
(j)	0.9547	0.7783	0.9229	0.8316	0.7047	0.9222	0.9985	0.7295	0.9079	0.7143	0.6043	0.9431	
(k)	0.9444	0.9404	0.8123	0.6738	0.5909	0.9472	0.9812	0.9535	0.7171	0.5786	0.4553	0.9097	
(l)	0.9339	0.6910	0.8313	0.8093	0.5279	0.9727	0.9987	0.5656	0.7326	0.6882	0.3759	0.9549	
(m)	0.7951	0.8359	0.4984	0.5963	0.7794	0.9058	0.9994	0.9800	0.4816	0.6213	0.9907	0.9994	
(n)	0.9230	0.8313	0.8788	0.8837	0.7062	0.9089	0.9949	0.7903	0.8932	0.8295	0.5666	0.9994	
(o)	0.9433	0.8273	0.9053	0.8657	0.9357	0.9021	0.9987	0.7802	0.8956	0.7895	0.9985	1	
(p)	0.9206	0.7397	0.9121	0.8647	0.8791	0.8945	1	0.6312	0.8879	0.7758	0.9968	1	
Mean	0.8778	0.7915	0.7873	0.7980	0.7803	0.9224	0.9392	0.7980	0.7810	0.7710	0.7964	0.9675	

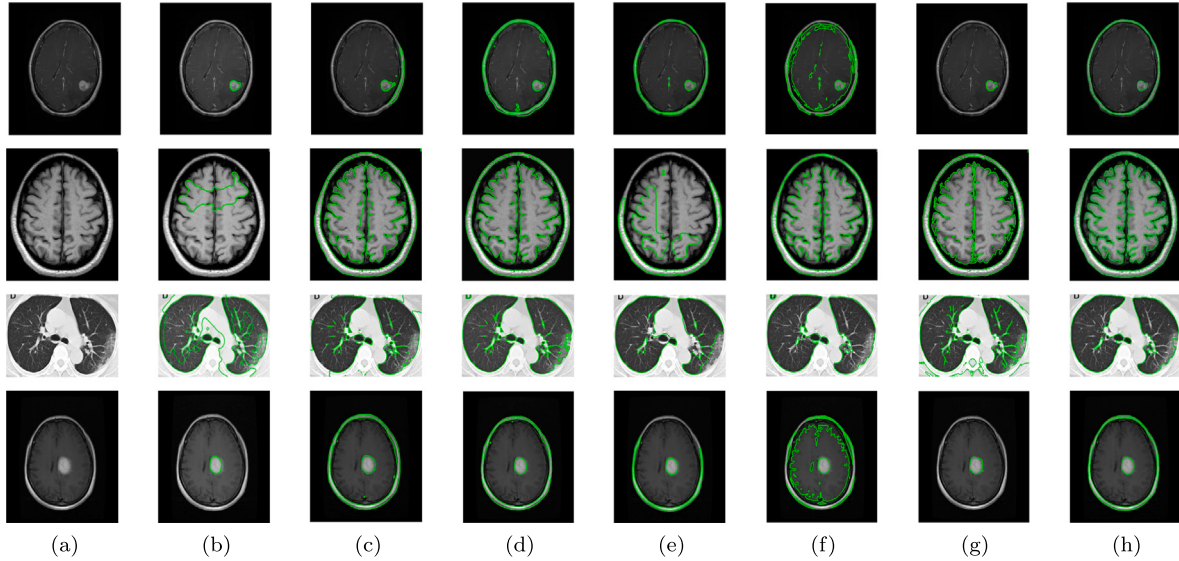


Fig. 6. The segmentation of four distinct MRI images was carried out using the ABC model, the LSACM model, the LBF model, the DRLSE-ADMM model, the HLFRA model, the ICTM model, and our model. The first to sixth columns align with the segmentation results of the ABC model, the LSACM model, the LBF model, the DRLSE-ADMM model, the HLFRA model, the ICTM model, and our model respectively.

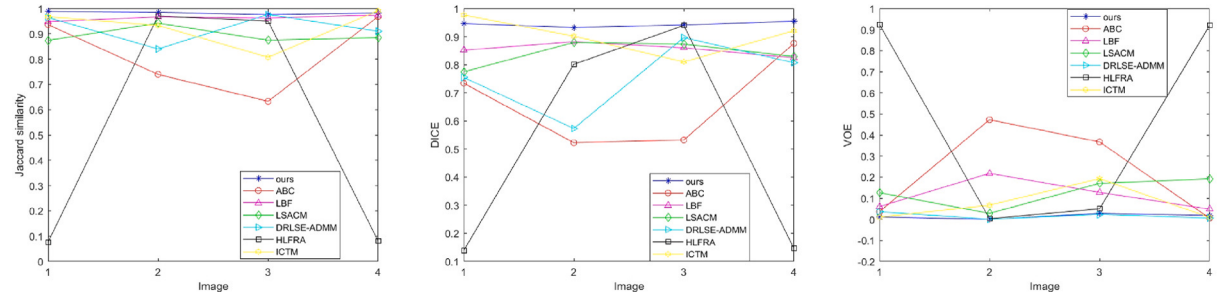


Fig. 7. The JS, Dice and VOE values obtained from our method for the images depicted in Fig. 6.

images alongside the corresponding segmentation outcomes obtained by introducing various types and intensities of noise. The first and second images were respectively added with Gaussian white noise with variances of 0.4 and 0.6, speckle noise with variances of 0.4 and 0.8 and salt and pepper noise with a variance of 0.8. The third image was added with Gaussian white noise with a variance of 0.3, salt and pepper noise with a variance of 0.5, and speckle noise with a variance of 0.3. It

is well known that the quality of an image decreases to varying degrees when severe noise is added. However, based on the experimental findings, it can be noted that the segmentation accuracy does not change significantly. Specifically, the third image demonstrates that even under the interference of noise and intensity inhomogeneity simultaneously, our method still achieves good segmentation results.

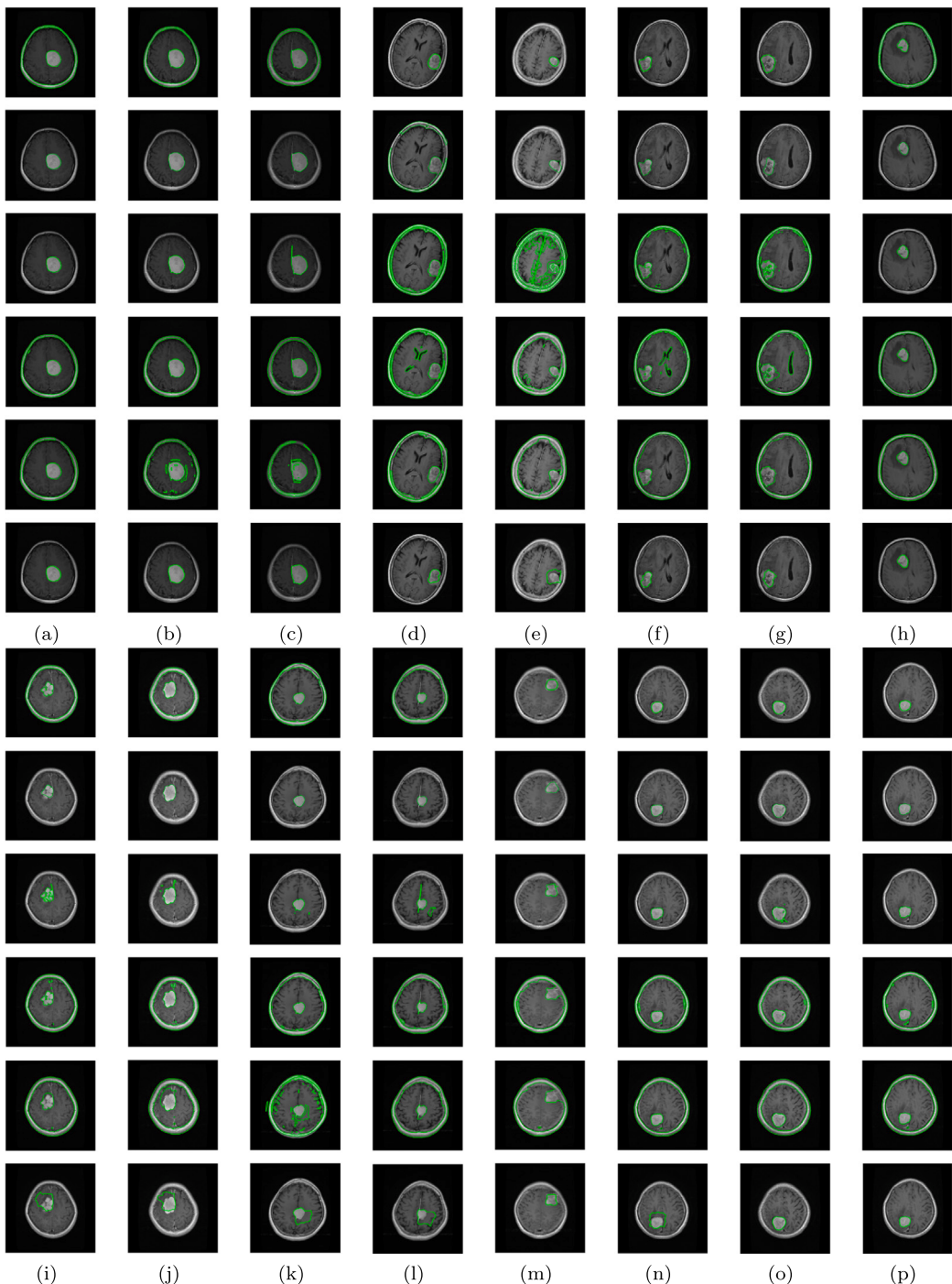


Fig. 8. The segmentation of sixteen distinct MRI images was executed using the ABC model, the ICTM model, the LBF model, the ALF model, the DRLSE model, and our model. The segmentation results are organized as follows: Row 1, 7: segmentation results of our model; Row 2, 8: segmentation results of the ABC model; Row 3, 9: segmentation results of the ICTM model; Row 4, 10: segmentation results of the LBF model; Row 5, 11: segmentation results of the ALF model; Row 6, 12: segmentation results of the DRLSE model.

4.7. Bias correction

To further illustrate the capacity of our method to correct bias field, four images with severe intensity inhomogeneity were subjected to illumination bias correction and subsequent segmentation. We set the parameters as follows: $\lambda_1 = \lambda_2 = \tau = 1$, $\tau_1 = 200$, $\beta = 0.25$, $\rho = 1.5$, and $\alpha = 200$. From the first column to the last column in Fig. 10, the sequence includes the original image with the initial contour, the outcome of segmenting the original image, the estimated bias field, and the result after bias field correction. From the correction results, it is apparent that our algorithm proficiently eliminates the intensity

Table 5

The JS values corresponding to the images using different initial contours are depicted in Fig. 11.

Image	(a)	(b)	(c)	(d)	(e)	(f)
JS	0.9633	0.9645	0.9647	0.9646	0.9634	0.965

inhomogeneity in the images and improves the overall image quality. Additionally, all four images demonstrate satisfactory segmentation results. Hence, our algorithm exhibits excellent bias field correction.

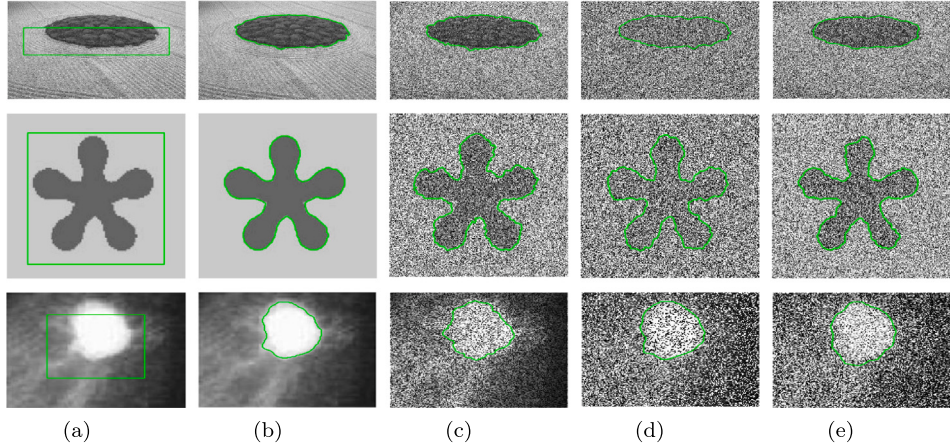


Fig. 9. Our model was applied to segment noisy images, and the segmentation results are as shown above. From left to right, they correspond to: original images with initial contours, segmentation results of the original images, images with added Speckle noise, images with added Salt and pepper noise, and images with added Gaussian noise.

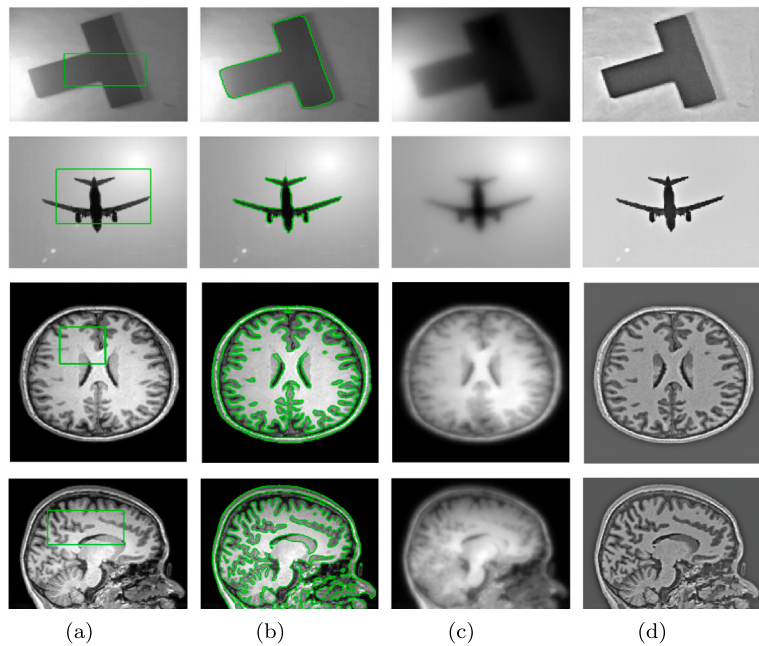


Fig. 10. Our model was employed to segment four distinct images affected by illumination bias. The segmentation process yielded the results shown above. From the first column to the last column, they correspond to: original images with initial contours, segmentation results of our model, estimated bias fields, and corrected images.

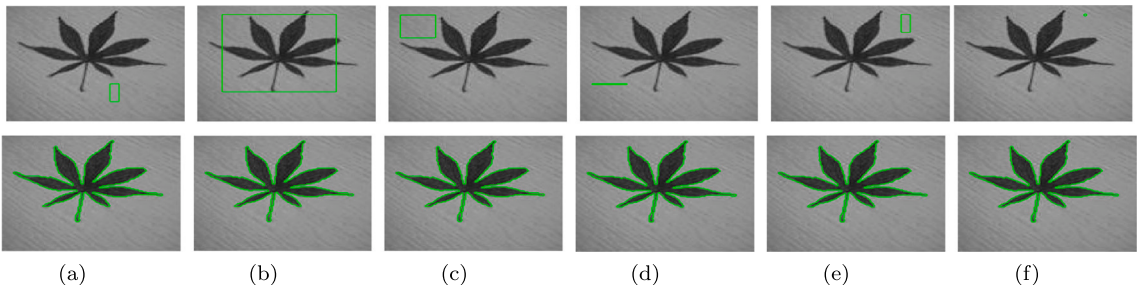


Fig. 11. The segmentation results of our model using different initial contours. Row 1 :original images with different initial contours. Row 2 : segmentation results obtained from our model.

4.8. Initial contour

With the intention of verifying the robustness of our algorithm with respect to the initial contour, our model was employed to images with six distinct initial contours, as depicted in Fig. 11. We set the

parameters as follows: $\lambda_1 = \lambda_2 = \tau = 1$, $\tau_1 = 80$, $\beta = 0.3$, $\rho = 2$, and $\alpha = 80$. In the first row of Fig. 11, the original images with various initial contours are displayed, while the second row exhibits the corresponding segmentation results. It is evident that our model produces consistent segmentation results across different initial contours.

The quantitative evaluation of the segmentation results is presented in Table 5. According to the Table 5, the JS values of our algorithm exhibit a consistent stability at approximately 0.964. This indicates that our algorithm has exceptional robustness to diverse initial contours and demonstrates excellent segmentation performance.

5. Conclusion

In this paper, we present a novel image segmentation model that utilizes the Retinex algorithm. Firstly, aiming to enhance the capability of our model to correct bias fields, we propose a prior constraint on the reflectance term. Secondly, we employ adaptive regularization constraints on the reflectance using the spatial information of the image. Experimental results demonstrate that these two assumptions improve the capability of our method to accurately segment images with blurry boundaries. Thirdly, to improve the intricate process of continuous re-initialization in traditional level set methods, we opt to adopt the binary level set assumption. Furthermore, extensive experiments were conducted on a diverse range of image types to thoroughly evaluate our approach, and the outcomes of the experiments indicate that our algorithm demonstrates good robustness to images with low contrast, images with intensity inhomogeneity and images with low illumination. In the forthcoming research, we will continue to boost the robustness of our algorithm to noise of various degrees.

CRediT authorship contribution statement

Wenqi Zhao: Conceptualization, Methodology, Validation, Formal analysis, Investigation, Data curation, Writing – original draft, Writing – review & editing, Visualization. **Jiacheng Sang:** Software, Resources, Investigation, Data curation, Writing – original draft, Writing – review & editing. **Yonglu Shu:** Supervision, Project administration, Writing – review & editing. **Dong Li:** Funding acquisition.

Declaration of competing interest

The authors declare that they have no known competing financial interests or personal relationships that could have appeared to influence the work reported in this paper.

Data availability

Data will be made available on request.

Acknowledgments

The presented work was supported by the National Science and Technology Innovation 2030 of China Next-Generation Artificial Intelligence Major Project (Grant No. 2018AAA0101800); Innovation Group Science Fund of Chongqing Natural Science Foundation, China (No. cstc2019jcyj-cxtx0003).

References

- Bao, L., Zhou, X., Zheng, B., Yin, H., Zhu, Z., Zhang, J., et al. (2023). Aggregating transformers and CNNs for salient object detection in optical remote sensing images. *Neurocomputing*, 553(C), <http://dx.doi.org/10.1016/j.neucom.2023.126560>.
- Cai, R., & Chen, Z. (2023). Brain-like Retinex: A biologically plausible Retinex algorithm for low light image enhancement. *Pattern Recognition*, 136, Article 109195. <http://dx.doi.org/10.1016/j.patcog.2022.109195>.
- Cai, Q., Liu, H., Zhou, S., Sun, J., & Li, J. (2018). An adaptive-scale active contour model for inhomogeneous image segmentation and bias field estimation. *Pattern Recognition*, 82, 79–93. <http://dx.doi.org/10.1016/j.patcog.2018.05.008>.
- Chan, T., & Vese, L. (2001). Active contours without edges. *IEEE Transactions on Image Processing*, 10(2), 266–277. <http://dx.doi.org/10.1109/83.902291>.
- Chen, D.-Q., & Cheng, L.-Z. (2012). Spatially adapted total variation model to remove multiplicative noise. *IEEE Transactions on Image Processing*, 21(4), 1650–1662. <http://dx.doi.org/10.1109/TIP.2011.2172801>.
- Cheng, M.-H., Huang, T.-Z., Zhao, X.-L., Ma, T.-H., & Huang, J. (2019). A variational model with hybrid hyper-Laplacian priors for Retinex. *Applied Mathematical Modelling*, 66, 305–321. <http://dx.doi.org/10.1016/j.apm.2018.09.022>.
- Du, S., Zhao, M., Liu, Y., You, Z., Shi, Z., Li, J., et al. (2023). Low-light image enhancement and denoising via dual-constrained Retinex model. *Applied Mathematical Modelling*, 116, 1–15. <http://dx.doi.org/10.1016/j.apm.2022.11.022>.
- Eshedoglu, S., & Tsai, Y.-H. R. (2006). Threshold dynamics for the piecewise constant Mumford–Shah functional. *Journal of Computational Physics*, 211(1), 367–384. <http://dx.doi.org/10.1016/j.jcp.2005.05.027>.
- Fang, J., Liu, H., Zhang, L., Liu, J., & Liu, H. (2021). Region-edge-based active contours driven by hybrid and local fuzzy region-based energy for image segmentation. *Information Sciences*, 546, 397–419. <http://dx.doi.org/10.1016/j.ins.2020.08.078>.
- Fu, X., Liao, Y., Zeng, D., Huang, Y., Zhang, X.-P., & Ding, X. (2015). A probabilistic method for image enhancement with simultaneous illumination and reflectance estimation. *IEEE Transactions on Image Processing*, 24(12), 4965–4977. <http://dx.doi.org/10.1109/TIP.2015.2474701>.
- Goldstein, T., & Osher, S. (2009). The split Bregman method for L1-regularized problems. *SIAM Journal on Imaging Sciences*, 2(2), 323–343. <http://dx.doi.org/10.1137/080725891>.
- Guo, X., Li, Y., & Ling, H. (2017). LIME: Low-light image enhancement via illumination map estimation. *IEEE Transactions on Image Processing*, 26(2), 982–993. <http://dx.doi.org/10.1109/TIP.2016.2639450>.
- Jia, F., Wong, H. S., Wang, T., & Zeng, T. (2023). A reflectance re-weighted Retinex model for non-uniform and low-light image enhancement. *Pattern Recognition*, 144, Article 109823. <http://dx.doi.org/10.1016/j.patcog.2023.109823>.
- Jin, Z., Wu, Y., Min, L., & Ng, M. K. (2020). A Retinex-based total variation approach for image segmentation and bias correction. *Applied Mathematical Modelling*, 79, 52–67. <http://dx.doi.org/10.1016/j.apm.2019.11.005>.
- Lan, X., Shen, H., Zhang, L., & Yuan, Q. (2014). A spatially adaptive Retinex variational model for the uneven intensity correction of remote sensing images. *Signal Processing*, 101, 19–34. <http://dx.doi.org/10.1016/j.sigpro.2014.01.017>.
- Land, E. H. (1977). The Retinex theory of color vision. *Scientific American*, 237(6), 108–128. <http://dx.doi.org/10.1038/scientificamerican1277-108>.
- Li, Y., Cao, G., Wang, T., Cui, Q., & Wang, B. (2020). A novel local region-based active contour model for image segmentation using Bayes theorem. *Information Sciences*, 506, 443–456. <http://dx.doi.org/10.1016/j.ins.2019.08.021>.
- Li, C., Kao, C.-Y., Gore, J. C., & Ding, Z. (2008). Minimization of region-scalable fitting energy for image segmentation. *IEEE Transactions on Image Processing*, 17(10), 1940–1949. <http://dx.doi.org/10.1109/TIP.2008.2002304>.
- Li, C., Xu, C., Gui, C., & Fox, M. D. (2010). Distance regularized level set evolution and its application to image segmentation. *IEEE Transactions on Image Processing*, 19(12), 3243–3254. <http://dx.doi.org/10.1109/TIP.2010.2069690>.
- Lie, J., Lysaker, M., & Tai, X.-C. (2006). A binary level set model and some applications to Mumford–Shah image segmentation. *IEEE Transactions on Image Processing*, 15(5), 1171–1181. <http://dx.doi.org/10.1109/TIP.2005.863956>.
- Liu, Y., He, C., Gao, P., Wu, Y., & Ren, Z. (2019). A binary level set variational model with L1 data term for image segmentation. *Signal Processing*, 155, 193–201. <http://dx.doi.org/10.1016/j.sigpro.2018.08.017>.
- Luo, S., Tai, X.-C., Huo, L., Wang, Y., & Glowinski, R. (2019). Convex shape prior for multi-object segmentation using a single level set function. In *2019 IEEE/CVF international conference on computer vision* (pp. 613–621). <http://dx.doi.org/10.1109/ICCV.2019.00070>.
- Ma, D., Liao, Q., Chen, Z., Liao, R., & Ma, H. (2019). Adaptive local-fitting-based active contour model for medical image segmentation. *Signal Processing: Image Communication*, 76, 201–213. <http://dx.doi.org/10.1016/j.image.2019.05.006>.
- Ma, W., & Osher, S. (2012). A TV Bregman iterative model of Retinex theory. *Inverse Problems and Imaging*, 6, 697–708. <http://dx.doi.org/10.3934/ipi.2012.6.697>.
- Mumford, D., & Shah, J. (1989). Optimal approximations by piecewise smooth functions and associated variational problems. *Communications on Pure and Applied Mathematics*, 42, 577–685. <http://dx.doi.org/10.1002/cpa.3160420503>.
- Ng, M. K., & Wang, W. (2011). A total variation model for Retinex. *SIAM Journal on Imaging Sciences*, 4(1), 345–365. <http://dx.doi.org/10.1137/100806588>.
- Obeso, A. M., Benois-Pineau, J., García Vázquez, M. S., & Álvaro Ramírez Acosta, A. (2022). Visual vs internal attention mechanisms in deep neural networks for image classification and object detection. *Pattern Recognition*, 123, Article 108411. <http://dx.doi.org/10.1016/j.patcog.2021.108411>.
- Ren, X., Yang, W., Cheng, W.-H., & Liu, J. (2020). LR3M: Robust low-light enhancement via low-rank regularized Retinex model. *IEEE Transactions on Image Processing*, 29, 5862–5876. <http://dx.doi.org/10.1109/TIP.2020.2984098>.
- Wali, S., Li, C., Imran, M., Shakoor, A., & Basit, A. (2023). Level-set evolution for medical image segmentation with alternating direction method of multipliers. *Signal Processing*, 211, Article 109105. <http://dx.doi.org/10.1016/j.sigpro.2023.109105>.
- Wang, G., Dong, Q., Pan, Z., Zhang, W., Duan, J., Bai, L., et al. (2016). Retinex theory based active contour model for segmentation of inhomogeneous images. *Digital Signal Processing*, 50, 43–50. <http://dx.doi.org/10.1016/j.dsp.2015.12.011>.
- Wang, X.-F., Huang, D.-S., & Xu, H. (2010). An efficient local Chan–Vese model for image segmentation. *Pattern Recognition*, 43(3), 603–618. <http://dx.doi.org/10.1016/j.patcog.2009.08.002>.
- Wang, D., & Wang, X.-P. (2022). The iterative convolution–thresholding method (ICTM) for image segmentation. *Pattern Recognition*, 130, Article 108794. <http://dx.doi.org/10.1016/j.patcog.2022.108794>.

- Wang, L., Zhang, L., Yang, X., Yi, P., & Chen, H. (2020). Level set based segmentation using local fitted images and inhomogeneity entropy. *Signal Processing*, 167, Article 107297. <http://dx.doi.org/10.1016/j.sigpro.2019.107297>.
- Wang, F., Zhao, X.-L., & Ng, M. K. (2016). Multiplicative noise and blur removal by framelet decomposition and l_1 -based L-curve method. *IEEE Transactions on Image Processing*, 25(9), 4222–4232. <http://dx.doi.org/10.1109/TIP.2016.2583793>.
- Wen, L., Cheng, Y., Fang, Y., & Li, X. (2023). A comprehensive survey of oriented object detection in remote sensing images. *Expert Systems with Applications*, 224, Article 119960. <http://dx.doi.org/10.1016/j.eswa.2023.119960>.
- Weng, G., Dong, B., & Lei, Y. (2021). A level set method based on additive bias correction for image segmentation. *Expert Systems with Applications*, 185, Article 115633. <http://dx.doi.org/10.1016/j.eswa.2021.115633>.
- Weng, G., & Yan, X. (2020). Robust active contours driven by order-statistic filtering energy for fast image segmentation. *Knowledge-Based Systems*, 197, Article 105882. <http://dx.doi.org/10.1016/j.knosys.2020.105882>.
- Wu, Y., Li, M., Zhang, Q., & Liu, Y. (2018). A Retinex modulated piecewise constant variational model for image segmentation and bias correction. *Applied Mathematical Modelling*, 54, 697–709. <http://dx.doi.org/10.1016/j.apm.2017.10.018>.
- Yang, Y., Shu, X., Wang, R., Feng, C., & Jia, W. (2020). Parallelizable and robust image segmentation model based on the shape prior information. *Applied Mathematical Modelling*, 83, 357–370. <http://dx.doi.org/10.1016/j.apm.2020.02.028>.
- Yang, Y., Wang, R., & Feng, C. (2020). Level set formulation for automatic medical image segmentation based on fuzzy clustering. *Signal Processing: Image Communication*, 87, Article 115907. <http://dx.doi.org/10.1016/j.image.2020.115907>.
- Yang, Y., Wang, R., Shu, X., Feng, C., Xie, R., Jia, W., et al. (2021). Level set framework with transcendental constraint for robust and fast image segmentation. *Pattern Recognition*, 117, Article 107985. <http://dx.doi.org/10.1016/j.patcog.2021.107985>.
- Yang, B., Zhao, H., Cao, L., Liu, H., Wang, N., & Li, H. (2023). Retinal image enhancement with artifact reduction and structure retention. *Pattern Recognition*, 133, Article 108968. <http://dx.doi.org/10.1016/j.patcog.2022.108968>.
- Zhang, K., Zhang, L., Lam, K.-M., & Zhang, D. (2016). A level set approach to image segmentation with intensity inhomogeneity. *IEEE Transactions on Cybernetics*, 46(2), 546–557. <http://dx.doi.org/10.1109/TCYB.2015.2409119>.
- Zhang, K., Zhang, L., Song, H., & Zhang, D. (2013). Reinitialization-free level set evolution via reaction diffusion. *IEEE Transactions on Image Processing*, 22(1), 258–271. <http://dx.doi.org/10.1109/TIP.2012.2214046>.
- Zhou, S., Wang, J., Zhang, S., Liang, Y., & Gong, Y. (2016). Active contour model based on local and global intensity information for medical image segmentation. *Neurocomputing*, 186, 107–118. <http://dx.doi.org/10.1016/j.neucom.2015.12.073>.
- Zhou, M., Wu, X., Wei, X., Xiang, T., Fang, B., & Kwong, S. (2023). Low-light enhancement method based on a Retinex model for structure preservation. *IEEE Transactions on Multimedia*, 1–13. <http://dx.doi.org/10.1109/TMM.2023.3268867>.
- Zhu, J., Zeng, Y., Xu, H., Li, J., Tian, S., & Liu, H. (2021). Maximum a posterior based level set approach for image segmentation with intensity inhomogeneity. *Signal Processing*, 181, Article 107896. <http://dx.doi.org/10.1016/j.sigpro.2020.107896>.
- Zosso, D., An, J., Stevick, J., Takaki, N., Weiss, M., Slaughter, L. S., et al. (2017). Image segmentation with dynamic artifacts detection and bias correction. *Inverse Problems and Imaging*, 11, 577–600. <http://dx.doi.org/10.3934/ipi.2017027>.